Thermal-wave radar: A novel subsurface imaging modality with extended depth-resolution dynamic range

Nima Tabatabaei[a] and Andreas Mandelis[b]
Department of Mechanical and Industrial Engineering, Center for Advanced Diffusion-Wave Technologies (CADIFT), University of Toronto, Toronto, Ontario M5S 3G8, Canada

(Received 4 December 2008; accepted 16 February 2009; published online 18 March 2009)

Combining the ideas behind linear frequency modulated continuous wave radars and frequency domain photothermal radiometry (PTR), a novel PTR method is introduced. Analytical solutions to the heat diffusion problem for both opaque and transparent solids are provided. Simulations and experimental results suggest a significant improvement in the dynamic range when using the thermal-wave radar (TWR) instead of conventional PTR. A practical TWR image resolution augmentation method is proposed. © *2009 American Institute of Physics.*
[DOI: 10.1063/1.3095560]

I. INTRODUCTION

Medical and nondestructive testing applications of pulsed and continuously modulated (frequency-domain) photothermal radiometry methods (PPTR and FDPTR, respectively) have been the topic of many studies since the early 1980s.[1–9] PPTR (Ref. 3) uses short duration excitation sources with relatively high peak power while FDPTR (henceforth denoted simply by PTR)[1,2,4] incorporates low energy excitation sources with long duty cycles. Both methods can be carried out in transmission[1,4] and backscattering[2,3] modes, but the backscattering mode attracted more attention since having access to the other side of a specimen is not always possible. PPTR uses high power short-pulse laser sources to ensure detection of high signal-to-noise ratio (SNR) photothermal cooling profiles. This is a major drawback that limits the usefulness of PPTR, especially for samples with low laser-damage thresholds (i.e., biological samples). Moreover, the wideband nature of PPTR detection, laser pulse jitter, and high cost of pulsed laser sources limit the applications of PPTR even further. In contrast, PTR uses inexpensive low-energy excitation sources that are modulated at one or more frequencies. Almost all the early researches using PTR were focused on performing nondestructive tests on metals,[1] polymers,[4] and semiconductors.[5] However, in the last decade, many efforts have been made to investigate the medical applications of PTR.[6–9] Mandelis and co-workers[6,7] were first to apply PTR to the detection of human dental demineralization lesions and defects. They were able to detect carious lesions in dentin and enamel fissures. Recently, preliminary results by Kwan *et al.*[8] indicated that PTR also has the potential to detect osteoporotic bone loss. The most important drawback of medical PTR is its limited depth detection range. Due to significant damping of thermal waves and exposure limitations of the excitation source power (from a safety perspective), PTR is mostly used to detect subsurface defects in solids and hard tissues with the interrogated surface directly exposed to laser radiation. It is the intention of this paper to propose a novel photothermal radiometry methodology to improve both the dynamic range and the depth resolution of PTR. This so-called thermal-wave radar (TWR) method is able to detect inhomogeneities far beneath the effective detection range of conventional PTR. TWR has the potential to be used in biomedical applications, since it can detect the delay time between excitation and response thermal waveforms, which is directly related to the depth of the absorber (i.e., chromophores). In the following sections, TWR radar principles, TWR theory, analytical solutions to the heat diffusion boundary-value problem along with simulations, and experimental results are presented and discussed.

II. RADAR PRINCIPLES

In radar science, detecting a signal through a noisy channel has always been a challenge and, until now, many researches have been carried out to introduce new signal recognition methodologies that implement high SNR values. In the mid-1940s Van Vleck and Middleton[10] realized that, by using a special kind of linear filters (known as matched filters), one can detect a preknown signal waveform in a highly noisy channel. Matched filters were designed based on the preknown waveform, such that they maximized the output when a delayed replica of the waveform was passed through the channel.[11,12] The well-known cross-correlation technique is a special case of a matched filter, extensively used for signal detection, especially in continuous wave (CW) radars. CW radars use different types of phase compression methods, such as linear frequency modulation (LFM), in order to augment both the SNR and range resolution.[13] A linear frequency modulated waveform (otherwise known as a linear chirp), such as a LFM laser beam, can be expressed as

$$f(t) = Q_0 \sin[2\pi f_1(t)t], \tag{1a}$$

[a]Electronic mail: nimat@mie.utoronto.ca.
[b]Author to whom correspondence should be addressed. Electronic mail: mandelis@mie.utoronto.ca.

$$f_1(t) = f_s + Bt, \tag{1b}$$

$$B = \frac{(f_e - f_s)}{2T}, \tag{1c}$$

$$\varphi(t) = \frac{\partial[f_1(t)t]}{\partial t} = f_s + 2Bt = f_s + \frac{(f_e - f_s)}{T}t, \tag{1d}$$

where Q_0, $f_1(t)$, f_s, f_e, B, T, and $\varphi(t)$ are the modulated waveform intensity, frequency modulation function (chirp), chirp start frequency, chirp end frequency, chirp sweep rate, chirp time, and waveform instantaneous phase, respectively.

The cross-correlation of a signal with its delayed replica (i.e., a backscattered echo) will result in a sinc type waveform, $\mathrm{sinc}(x) = \sin(x)/x$, with the main peak centered on the corresponding delay time. In the acoustic or other propagating wave cases, the distance between the object and receiver is directly proportional to the calculated peak delay time τ_p and can be estimated using the wave speed in the medium. Moreover, through signal windowing, one can further increase the SNR and the detection range of the LFMCW radar by reducing the side lobes that are associated with the cross-correlation operation. In order to calculate the cross-correlation of two signals $h(t)$ and $s(t)$, i.e., reference and reflected signals respectively, one can either use Eq. (2a) or use the more convenient Fourier transform frequency domain formula, Eq. (2b).[14]

$$(s \times h)(\tau) = \int_{-\infty}^{\infty} s(t)h(t+\tau)dt \tag{2a}$$

$$(s \times h)(\tau) = \Im^{-1}\{S(\omega)[H(\omega)W(\omega)]^*\} \tag{2b}$$

$$S(\omega) = \Im\{s(t)\} \quad \text{and} \quad H(\omega) = \Im\{h(t)\}. \tag{2c}$$

Here $W(\omega)$ is the frequency domain windowing function for reducing the side lobes and * and $\Im$ denote the complex conjugate and Fourier transform operators, respectively.

Compared to pulsed radars, frequency modulated CW radars transmit higher energy within their long duty cycle and simultaneously attain the resolution of short pulsed radars by means of the cross-correlation method. LFM does not change the energy of the input signal; however, it puts the input signal energy under the main lobe of the matched-filter output (the sinc function), which will result in an increase in the maximum value of the filter output. It can be shown that matched filters are the optimal linear filters for maximizing the SNR in the presence of stochastic noise.[12]

The energy within a certain frequency range of the spectrum can be obtained using the energy spectral density (ESD) function. This function has the unit of energy/hertz and can be calculated as

$$\Phi(\omega) = \frac{G(\omega)G^*(\omega)}{2\pi}, \tag{3}$$

where $G(\omega) = \Im\{S(t)\}$ and $S(t)$ is the received signal.

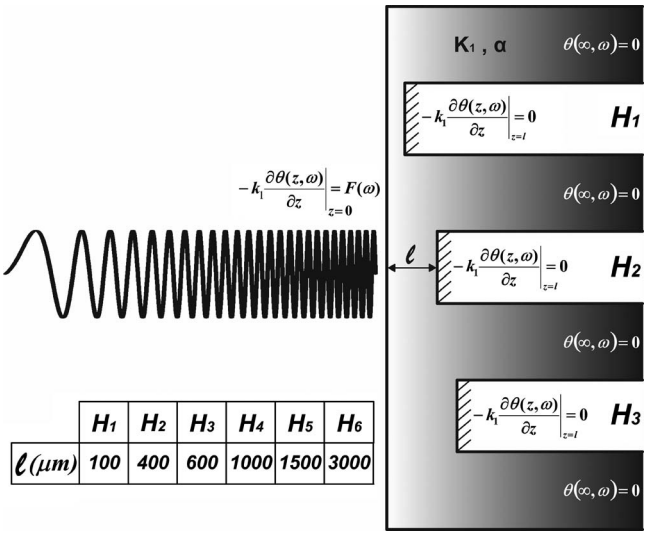

FIG. 1. A schematic of the steel block used in this study. The table inset indicates the actual thicknesses (l) (distances from the surface) for the six drilled holes (three holes in each row).

III. THEORY OF THERMAL-WAVE RADAR

A. Opaque solids

In this section, an analytical model for the TWR method is presented. Since, in our experiments, the laser beam diameter at sample surface is much larger than the estimated thermal diffusion length, it is reasonable to assume a one-dimensional (1D) heat flow in the solid. This assumption has also been made elsewhere.[15] Therefore, for a finitely thick sample, by assuming an insulated rear surface and a time dependent heat flux on the front surface (Fig. 1), a simplified version of the associated heat transfer problem can be obtained. In order to solve the boundary value problem, we apply the infinite integral Fourier transform to the time domain problem, assuming a zero value for the ac temperature for $t < 0$. As a result, the frequency domain boundary-value problem can be formulated as follows:

$$\frac{\partial^2\theta(z,\omega)}{\partial z^2} - \frac{i\omega}{\alpha}\theta(z,\omega) = 0, \tag{4}$$

$$-k_1\frac{\partial\theta(z,\omega)}{\partial z}\bigg|_{z=0} = \Im\{f(t)\} = F(\omega), \tag{5}$$

$$-k_1\frac{\partial\theta(z,\omega)}{\partial z}\bigg|_{z=l} = 0, \tag{6}$$

$$\theta(z,\omega) = T(z,\omega) - T_\infty, \tag{7}$$

where α, k_1, $F(\omega)$, and T_∞ are thermal diffusivity, thermal conductivity, the incident LFM laser beam spectrum, and sample equilibrium temperature, respectively. Equation (4) is a homogeneous second order ordinary differential equation that can be solved by finding the solutions of the corresponding characteristic equation. Furthermore, by applying the boundary conditions [Eqs. (5) and (6)] to the general solution [Eq. (8)], one can find the final solution to the frequency domain heat diffusion problem as

$$\theta(z,\omega) = A(\omega,l)\exp(\sigma z) + B(\omega,l)\exp(-\sigma z), \tag{8}$$

$$A(\omega,l) = \frac{F(\omega)}{k_1\sigma}\frac{\exp(-2l\sigma)}{1-\exp(-2l\sigma)}, \tag{9}$$

$$B(\omega,l) = \frac{F(\omega)}{k_1\sigma}\frac{\exp(-2l\sigma)}{1-\exp(-2l\sigma)}. \tag{10}$$

Here $\sigma=(1+i)/\mu$ is the complex wave number, $\theta(z,\omega)$ is the frequency domain ac temperature (thermal-wave) field, and $\mu=\sqrt{2\alpha/\omega}$ is the thermal diffusion length. One can find the time domain ac temperature field inside a finite thickness sample by taking the numerical inverse Fourier transform of Eq. (8). Thermal diffusion length plays a key role in the present methodology as it indicates the approximate maximum imaging depth at a specific modulation frequency. By definition, as the modulation frequency increases, the thermal diffusion length decreases. As a result, when using a LFM laser beam, we do not expect the high frequency components of a chirp to penetrate as deeply as their low frequency counterparts.

In photothermal radiometry, the thermal response of a given sample to a time dependent illumination is detected through thermal infrared (Planck) radiation originating in the irradiated region. In this case, the infrared detector signal can be estimated as[16]

$$S(t) = \gamma\left\{\Im^{-1}\left[\mu_{\mathrm{IR}}\int_0^l \theta(z,\omega)\exp(-\mu_{\mathrm{IR}}z)dz\right]\right\}, \tag{11}$$

where μ_{IR} is the infrared absorption coefficient over the detection wavelength range and γ is an instrumental constant which will henceforth be considered as 1.

Inserting Eq. (8) into Eq. (11) and integrating through the sample thickness, the radiometric signal can be found as

$$S(t) = \Im^{-1}[S(\omega)] = \Im^{-1}\left\{\left[\frac{A(\omega,l)\mu_{\mathrm{IR}}}{\sigma-\mu_{\mathrm{IR}}}\right][e^{l(\sigma-\mu_{\mathrm{IR}})}-1] + \left[\frac{B(\omega,l)\mu_{\mathrm{IR}}}{\sigma+\mu_{\mathrm{IR}}}\right][1-e^{-l(\sigma+\mu_{\mathrm{IR}})}]\right\}. \tag{12}$$

In view of the fact that this method was experimentally applied to a geometry similar to Fig. 1 involving subsurface drilled holes in a steel block, a fully optically opaque solid, the infrared absorption coefficient of steel can be considered to be infinity due to photothermal saturation. Therefore, letting $\mu_{\mathrm{IR}}\to\infty$ in Eq. (12), the infrared detector signal in a sample having a finite thickness l can be obtained as

$$S(t) = \Im^{-1}[A(\omega,l)+B(\omega,l)]. \tag{13}$$

As a result of thermal-wave damping, even a finite thickness sample can behave as semi-infinite with high frequency thermal waves. The simplest thermal-wave case of a semi-infinite solid can be obtained analytically from the boundary-value problem of Eqs. (4)–(7) upon replacing the boundary condition at $z=l$ with boundedness at $z\to\infty$, i.e., $\theta(\infty,\omega)=0$. Subsequently, the resulting frequency domain temperature field $\theta(z,\omega)$ and the radiometric signal spectrum can be obtained as

$$\theta(z,\omega) = C(\omega)\exp(-\sigma z), \tag{14}$$

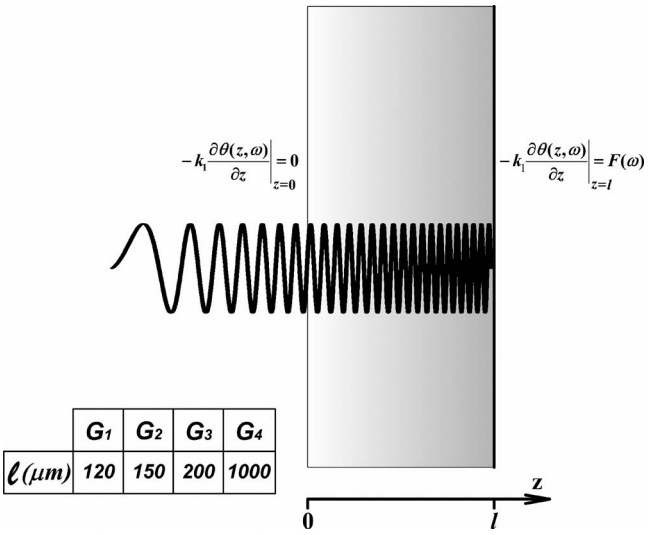

FIG. 2. A schematic of the glass samples used in this study. The table inset indicates the microscope slip sample thicknesses (l). Samples were coated on their back surface by an opaque coating.

$$C(\omega) = \frac{F(\omega)}{k_1\sigma}, \tag{15}$$

$$S(\omega) = \mu_{\mathrm{IR}}\int_0^\infty \theta(z,\omega)\exp(-\mu_{\mathrm{IR}}z)dz = \frac{C(\omega)\mu_{\mathrm{IR}}}{\sigma+\mu_{\mathrm{IR}}}. \tag{16}$$

Letting $\mu_{\mathrm{IR}}\to\infty$, Eq. (16) yields the well-known radiometric signal for metallic semi-infinite solids,

$$S(\omega) = C(\omega). \tag{17}$$

B. Transparent solids

The case of subsurface optical absorbers in the presence of absorbing or nonabsorbing overlayers is an important and challenging one for thermal waves because the damped nature of these diffusive waves from the underlayer tends to be dominated or completely masked by the conductive pathway across the overlayer and/or overlayer absorption contributions to the thermal wave detected at the front surface. To assess the performance of the TWR in this configuration, the heat diffusion problem was solved for a transparent solid (a glass), which is illuminated at its front surface ($z=0$) and coated with an opaque thin layer at its rear surface. In this case, optical radiation is absorbed on the back surface of the solid ($z=l$), Fig. 2. Subsequently, delayed with respect to the excitation beam, a (phase shifted) thermal wave is detected at the surface. The boundary-value problem of Eqs. (4)–(7) must be modified by assuming thermal insulation at the front surface and frequency modulated heat flux at $z=l$. The frequency domain temperature field and radiometric signal spectrum can then be obtained as

$$\theta(z,\omega) = E(\omega,l)[\exp(\sigma z)+\exp(-\sigma z)], \tag{18}$$

$$E(\omega,l) = \frac{F(\omega)}{k_1\sigma}\frac{1}{\exp(-l\sigma)-\exp(l\sigma)}, \tag{19}$$

$$S(\omega) = \frac{E(\omega,l)\mu_{IR}}{\sigma - \mu_{IR}}\{\exp[l(\sigma - \mu_{IR})] - 1\} + \frac{E(\omega,l)\mu_{IR}}{\sigma + \mu_{IR}}\{1 - \exp[-l(\sigma + \mu_{IR})]\}. \quad (20)$$

C. Thermal-wave radar response

Having modeled the radiometric signal spectrum for the special case of finite, semi-infinite, and transparent solids [$S(\omega)$ in Eqs. (13), (17), and (20)], the TWR output, $D(\tau)$, can be obtained by substituting the filter frequency response term in Eq. (2b), $H(\omega)$, with the applied optical heat source spectrum, $F(\omega)$, and the received signal spectrum term, $S(\omega)$, with the modeled radiometric signal spectrum of each foregoing solid sample and geometry:

$$D(\tau)_{\text{finite}} = \Im^{-1}\{[A(\omega,l) + B(\omega,l)][F(\omega)W(\omega)]^*\}, \quad (21)$$

$$D(\tau)_{\text{Semi-infinite}} = \Im^{-1}\{C(\omega)[F(\omega)W(\omega)]^*\}, \quad (22)$$

$$D(\tau)_{\text{Transparent}} = \Im^{-1}\left\{\left[\frac{E(\omega,l)\mu_{IR}}{\sigma - \mu_{IR}}(\exp[l(\sigma - \mu_{IR})] - 1) + \frac{E(\omega,l)\mu_{IR}}{\sigma + \mu_{IR}}(1 - \exp[-l(\sigma + \mu_{IR})])\right] \times [F(\omega)W(\omega)]^*\right\}. \quad (23)$$

D. Thermal-wave radar subtractive mode response

Unlike propagating hyperbolic wave fields, parabolic diffusive waves do not posses wave fronts. Furthermore, in these wave fields, the diffusive energy transport speeds are strongly dispersive.[17] As a result, in opaque solids, the coherent energy accumulation due to presence of underlayers can be effectively masked by the dominant front surface generated diffusive waves. One way to enhance the effect of underlayers is by omitting the effect of the dominant front surface generated diffusive waves through subtraction of the full radiometric signal of a semi-infinite opaque sample from that of a finite sample, provided that the same optical excitation waveform is used for both samples. Equation (24) illustrates this concept mathematically:

$$\Delta S(\omega) = [A(\omega,l) + B(\omega,l)] - C(\omega) = \frac{F(\omega)}{k_1\sigma}\frac{2\exp(-2l\sigma)}{1 - \exp(-2l\sigma)}. \quad (24)$$

Replacing the received signal spectrum term, $S(\omega)$, in Eq. (2b) with Eq. (24), one can find the TWR cross-correlation curve due to the coherent energy accumulation of underlayers as

$$\Delta D(\tau) = \Im^{-1}\left\{\frac{F(\omega)}{k_1\sigma}\frac{2\exp(-2l\sigma)}{1 - \exp(-2l\sigma)}[F(\omega)W(\omega)]^*\right\}. \quad (25)$$

Mathematically, Eq. (25) is the definition of the *TWR subtractive mode*. It will be shown in the following section that compared to TWR, the TWR subtractive mode is a more sensitive method for detecting deep inhomogeneities as the dominating fundamental forward diffusive term is eliminated.

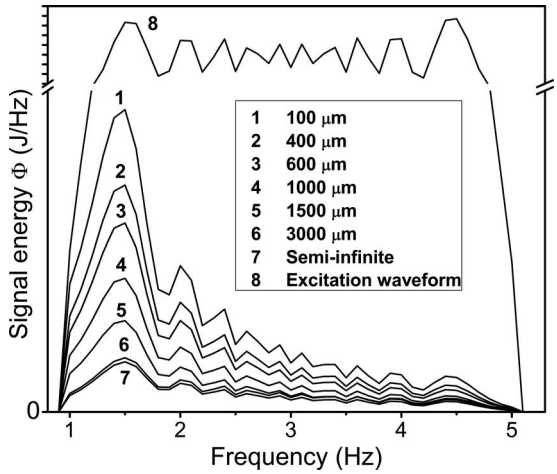

FIG. 3. The simulated ESD of the radiometric signal from a steel sample with several thicknesses and a semi-infinite surface. The ESD of the incident LFM excitation waveform is also included for comparison.

IV. THEORETICAL SIMULATIONS OF TWR

A. Opaque solids

Figure 3 depicts the ESD [Eq. (3)] of simulated radiometric signals [Eq. (13)] from steel samples with various thicknesses (l) along with the ESD of the simulated radiometric signal of a semi-infinite steel [Eq. (17)]. For the purpose of comparison, the ESD of the optical excitation waveform [Eq. (1a)] is also included. The spectral energy of the radiometric response from the steel sample surface can be divided into two parts: the energy due to excitation generated diffusive waves at the sample surface (surface energy absorption) and the coherently accumulated energy due to back-interface interacted thermal waves. Surface energy absorption increases the sample surface temperature and therefore produces a radiometric signal whose spectral energy distribution exhibits the damped behavior expected under the envelope of diffusion (a low pass filtering action). On the other hand, the energy due to back-interface interacted thermal waves in finitely thick opaque solids is delayed (phase shifted) with respect to the surface absorption energy part. In a semi-infinite sample, the radiometric signal energy (Fig. 3, curve 7) is only due to surface energy absorption and no delayed back-interface interacted thermal-wave contribution is expected. As a result, a relatively uniform ESD is observed, characterized by the diffusive low-pass filtering profile (damping).

The surface energy absorption part is also present in the ESD of finite thickness opaque samples. However, the interface interacted thermal-wave part of the ESD in these samples (both back and front interfaces) contribute to the resulting diffusion-wave frequency spectrum. In this sense, the delayed portion of the ESD (subtractive part) becomes a function of sample thickness and can be used as a sensitive parameter to distinguish various thicknesses. According to Fig. 3 as the sample thickness decreases the subtractive mode energy density increases. The energy increase is more

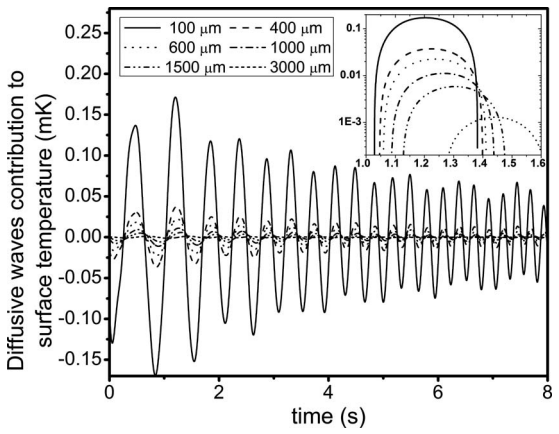

FIG. 4. The steel sample simulated surface temperature profile due to contribution of diffusive waves from several thicknesses with the fundamental forward thermal wave [Eq. (14)] subtracted. The semi-log figure inset magnifies the concept of delayed contribution due to an increase in sample thickness. The inset axes are the same as those of the figure.

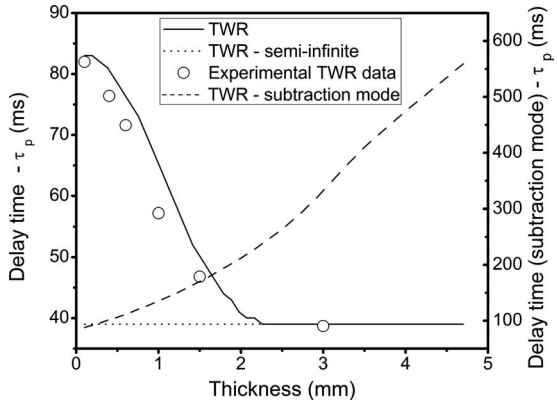

FIG. 6. Steel sample simulated TWR cross-correlation peak delay times for several thicknesses using TWR (solid line) and TWR in subtraction mode (dashed line). The dotted base line indicates the TWR delay time corresponding to a semi-infinite steel sample. Circles denote the normalized experimental data. Chirp bandwidth=1–5 Hz, chirp duration=10 s.

pronounced at lower frequencies as low frequency components are less damped during their propagation.

The concept of interface interacted (depleted or accumulated) thermal waves can be better understood from Fig. 4. This figure is the result of subtraction of the surface thermal waves of several finite thickness samples ($\Im^{-1}\{[\text{Eq. (8)}]|_{z=0}\}$) from that of a semi-infinite sample ($\Im^{-1}\{[\text{Eq. (14)}]|_{z=0}\}$). It can be observed that due to the damping behavior of thermal waves, as the sample thickness (l) increases, the coherent energy accumulation from the interface confinement to the detected thermal wave at the sample surface decreases. Moreover, this energy contribution becomes more delayed (Fig. 4 inset), as increasing the sample thickness results in increased transport distance for thermal waves. The concept of delayed contribution from subsurface thermophysical discontinuities is an important feature that can be used to distinguish various thicknesses and subsurface defects and lies at the heart of the TWR.

Figure 5 shows the simulated TWR/cross-correlation

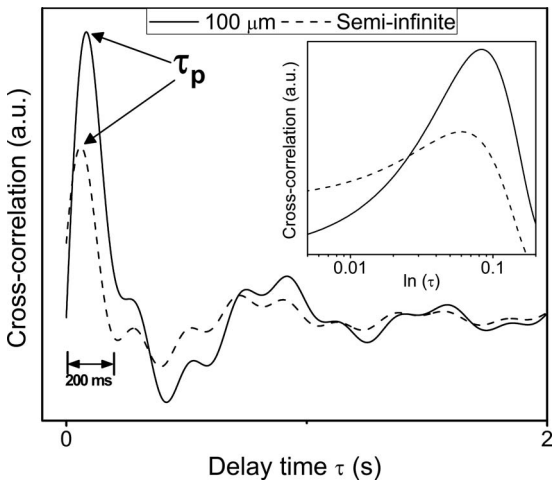

FIG. 5. Theoretical TWR signals for 100 μm thick and semi-infinite steel samples, using Eqs. (13) and (17). Chirp data: $T=10$ s, $f_s=1$ Hz, $f_e=5$ Hz, τ_p: TWR/cross-correlation peak delay time, and $\alpha=18.8\times10^{-6}$ m^2/s. Figure inset magnifies the time interval checked in main figure.

output signals for 100 μm thick and semi-infinite steel samples [Eqs. (21) and (22)]. It can be observed that as the steel sample thickness increases from 100 μm to infinity, the cross-correlation peak delay time (τ_p) decreases from 83 to 39 ms, as magnified in the figure inset. In addition, since the radiometric signal amplitude decreases as the sample thickness increases, the actual cross-correlation peak values are significantly different between these samples (32% difference). The theoretical TWR cross-correlation peak delay times as a function of sample thickness are plotted in Fig. 6 (solid line). In this plot, it is clearly seen that delay time decreases as the thickness increases. This is due to the fact that increasing the sample thickness dampens the contribution of thermal waves from depths other than the surface, such as confined thermal waves at the steel-air back interface. As a result, the ESD of the TWR signal becomes more similar to that of the semi-infinite sample (Fig. 3) and the TWR cross-correlation delay time approaches that of the semi-infinite sample (Fig. 6 dotted line), as expected. The cross-correlation peak delay time of a semi-infinite sample has a nonzero value (39 ms) due to the well-known time shift of the surface temperature oscillation with respect to the incident thermal-wave flux.[18]

The dashed line in Fig. 6 represents the theoretical variation of the TWR subtractive mode cross-correlation τ_p with sample thickness. Compared to the shallow saturation of the full TWR mode, this simulation clearly shows the capability of TWR in resolving delayed contributions from much deeper regions using the subtractive mode to enhance interface-interacted thermal waves. It can be observed that, as the sample thickness increases, the contribution is more delayed due to the increase in thermal-wave conduction distance. In order to obtain the subtractive radiometric signal in practice, the applied optical excitation waveforms for the finite and semi-infinite (reference) samples should be in phase, which is not possible experimentally when using analog function generators as was the case with our experiments. As a result, in this paper, the TWR in subtraction mode is only discussed theoretically.

Figure 7 shows the effect of excitation chirp properties

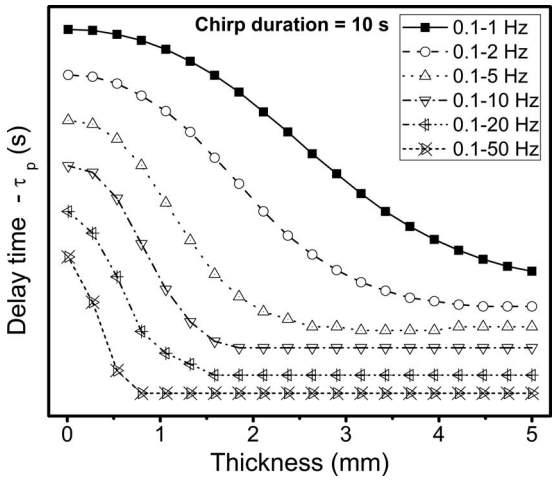

FIG. 7. Dependence of cross-correlation peak delay time τ_p on steel sample with chirp sweep rate as a parameter. The inset indicates the chirp bandwidth used for each line.

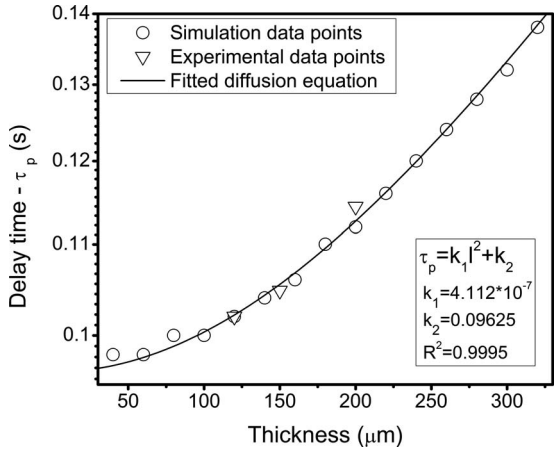

FIG. 9. Simulated TWR cross-correlation peak delay time for various glass sample thicknesses. Chirp data: f_s=0.1 Hz, f_e=5 Hz, duration=10 s, and $\alpha=0.45\times10^{-6}$ m^2/S. The diffusive equation is fitted to the simulation data. The fitting parameters [Eq. (28)] are available in the inset.

on the TWR depth detection range. This plot suggests that, at a fixed starting frequency (f_s), as frequency modulation sweep rate decreases, the theoretical detection range increases; however, at the same time the depth range resolution between shallow inhomogeneities decreases. This is manifested by smaller slopes at smaller thicknesses in Fig. 7. Therefore, it is possible to improve the TWR depth resolution by optimizing the chirp properties. However, in practice, reducing the chirp bandwidth toward low frequencies requires the use of expensive dc-coupled preamplifiers which is not always feasible.

B. Transparent solids

Figure 8 shows the simulated front and back surface TWR temperature profiles in a 1 mm thick glass sample. The front surface ac temperature profile lags behind the back surface ac temperature profile (Fig. 8 inset), as expected. This phase lag is directly related to the sample thickness and thermal properties of glass. Furthermore, not all frequency components in the optically generated heat flow can reach the front surface (detection plane) because the overlayer acts as an efficient low-pass filter. Moreover, the absolute (dc) temperature of the sample constantly increases as a result of the continuing inflow of thermal energy accumulating in the solid according to the theoretical model.

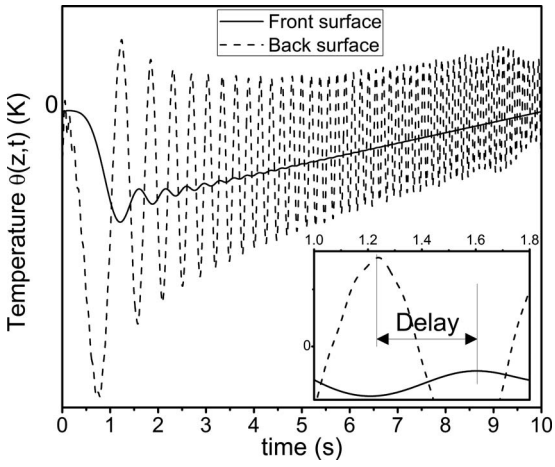

FIG. 8. ac temperature profile on front (solid line) and back (dashed line) surfaces of a 1 mm thick back-surface painted glass sample. The figure inset has the same axes as the main figure and illustrates the concept of delayed contribution of the two thermal waves.

Open circles in Fig. 9 depict the theoretical TWR cross-correlation peak delay times as a function of the thickness of the glass sample in the configuration of Fig. 2. When compared to the solid line in Fig. 6, a completely different trend is observed for the glass samples. In fact, the curve is more similar to that of the TWR subtractive mode (Fig. 6, dashed curve). The reason for this similarity is that in the case of transparent solids the ESD of the radiometric signal is only due to the contribution of thermal waves, which diffuse away from the absorbing back surface while the fundamental contribution from front-surface generated forward thermal waves is missing entirely.

The finite delay time τ_p at $l=0$ is a consequence of the heat flux-temperature rise delay discussed in conjunction with the baseline of Fig. 6. The theoretical simulations (Figs. 6 and 9) confirm that the matched filtering signal processing method used in the TWR is capable of measuring the delay time between the optical excitation waveform and the PTR response in both opaque and transparent solids. Subsequently, the thickness of the sample can be obtained by fitting the experimental data to the theoretical simulations.

C. PTR versus TWR

A different set of simulations was designed to verify the higher dynamic range of the TWR method compared to the conventional PTR method. In these simulations, the PTR (both phase and amplitude channels) and TWR responses of steel samples having thicknesses between 100 μm and 5 mm were simulated. In order to make the simulations more realistic, the radiometric signals were superposed with stochastic noise (SNR=1) before the signal processing step. Furthermore, ten iterations were used for each simulation to test the robustness of each method. Finally, the mean of the outputs (PTR amplitude and phase and cross-correlation

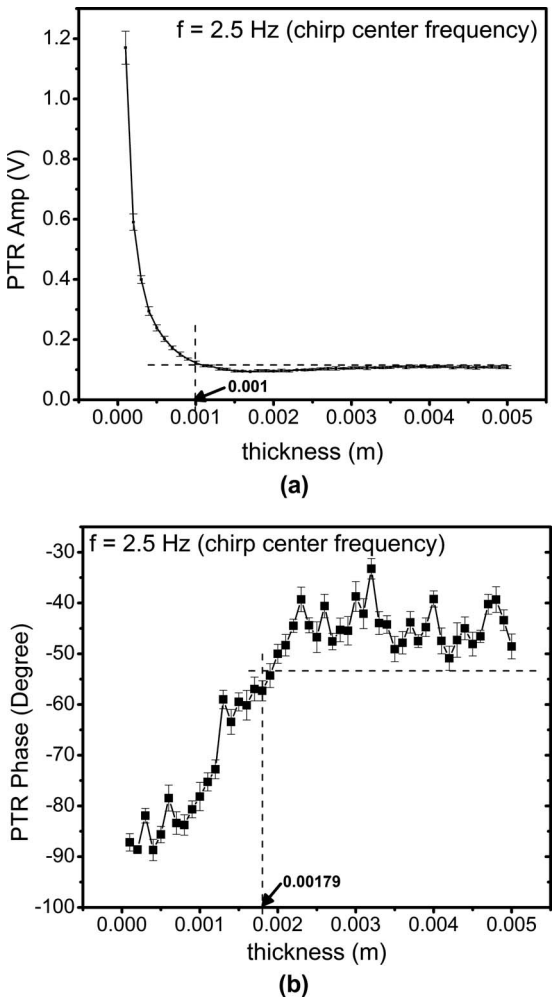

FIG. 10. Simulations of the variation in PTR signal with steel sample thickness. The input radiometric signal was superposed with stochastic noise (SNR=1) prior to signal processing. Each point was simulated ten times to measure the standard deviation. The maximum detection depth is indicated on the figure. (a) PTR amplitude. (b) PTR phase.

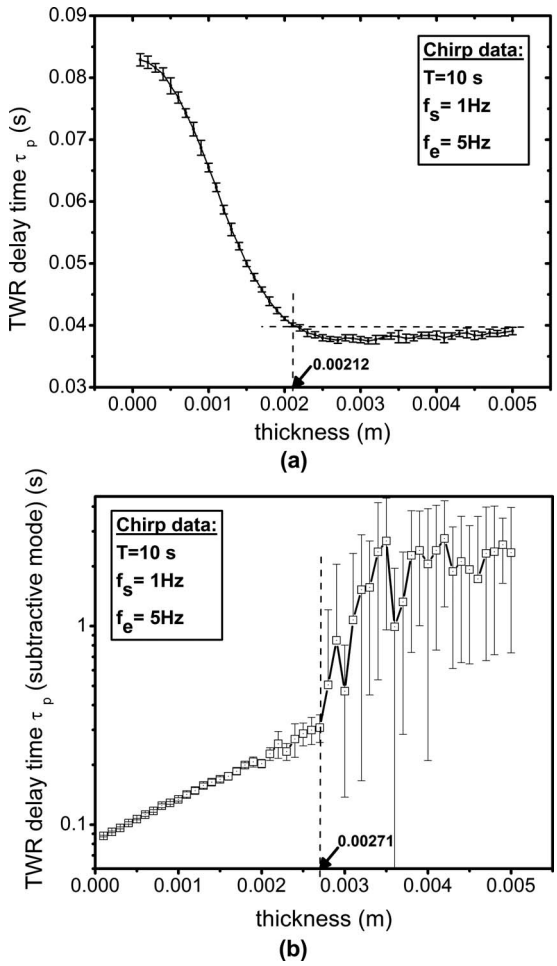

FIG. 11. Simulations of the variation in cross-correlation peak delay time τ_p with steel sample thickness: (a) TWR and (b) TWR subtractive mode. Simulation conditions are included in the figure insets.

peak delay times in both full TWR and TWR subtractive mode) was plotted against the sample thickness, where the error bars indicate the standard deviation for each simulation. Figures 10(a) and 10(b) show the simulation results of PTR amplitude and phase channels, respectively. It can be observed that the amplitude channel can only detect thicknesses unambiguously up to 1 mm. The phase channel, on the other hand, exhibits higher depth resolution and can detect thicknesses up to 1.79 mm. Figures 11(a) and 11(b) depict the simulation results of the TWR and TWR subtractive mode, respectively. In the case of the full TWR method, the dynamic range is improved by 112% compared to the PTR amplitude channel and 18.43% compared to the PTR phase channel. The TWR subtractive mode exhibits significantly higher depth resolution with a dynamic range enhancement of 171% over the PTR amplitude channel and 51.4% over the PTR phase channel. The dynamic range enhancement of TWR over PTR can be attributed to the high SNR in the matched-filtering method when used with phase compression techniques such as the LFM used in this work. Using the conventional radar SNR expressions for calculating the TWR SNR will result in a very high SNR value (four orders of magnitude higher than that of PTR), which cannot be realistic. The reason for this discrepancy is that the conventional radar formulas do not account for the damped nature of thermal waves. Therefore, a more realistic formula for both PTR and TWR is introduced as suggested by other investigators,[19]

$$\mathrm{SNR}_{(\mathrm{FDPTR,TWR})} = \frac{\mathrm{Output\ \ mean}_{(\mathrm{FDPTR,TWR})}}{\mathrm{Output\ \ standard\ \ deviation}_{(\mathrm{FDPTR,TWR})}}, \tag{26}$$

where the output of PTR can be either amplitude or phase and the output of TWR is the cross-correlation peak delay time. Using Eq. (25), the following values can be obtained for the simulation data depicted in Figs. 10 and 11:

$$\mathrm{SNR}_{\mathrm{FDPTR}}^{\mathrm{Amp}} = 27.96,$$

$$\mathrm{SNR}_{\mathrm{FDPTR}}^{\mathrm{Phase}} = 28.95,$$

$$\mathrm{SNR}_{\mathrm{TWR}} = 77.90.$$

The SNR of TWR is 178% higher than that of PTR amplitude channel and 169% higher than that of PTR phase channel. The experimental results further demonstrate the enhanced depth-resolution dynamic range of TWR compared to PTR.

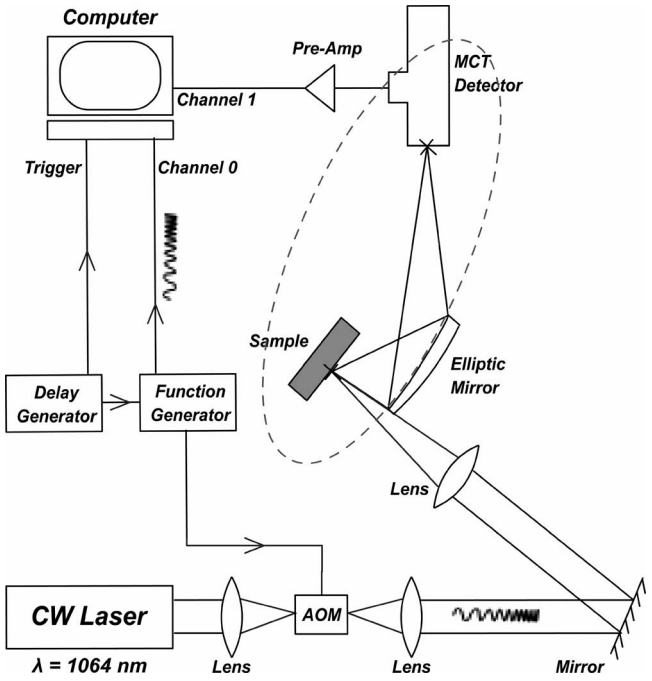

FIG. 12. Experimental setup of the TWR system embodied in a photothermal radiometric detection scheme. For details on each component, refer to the text.

V. MATERIALS AND EXPERIMENTAL

An AISI 1010 steel block with six 5 mm diameter blind holes located at various depths from the surface was used in this study (Fig. 1). The wall thicknesses above the holes l are shown in the inset of Fig. 1. Figure 12, schematically illustrates the experimental setup for the TWR system using the photothermal radiometric detection principle. A 1064 nm CW laser source (IPG Photonics) was frequency modulated by an acousto-optic modulator (AOM) (Neos Technologies). Modulation was done either at a single frequency or in a linear frequency sweep. The sample was fixed on a two-dimensional (2D) translation stage with its surface located at one focal point of an elliptic mirror. The black-body infrared radiation from the sample surface was collected at the other focal point of the mirror by a mercury cadmium telluride (MCT) infrared detector (Judson technologies). The MCT signal was first amplified by a preamplifier (PA-101, Judson Technologies) and then digitized by a high speed dual channel analog to digital converter (PCI-5122, National Instruments). The synchronization of the data acquisition software and the modulation systems was carried out through a delay generator (DG535, Stanford Research systems). The delay generator simultaneously triggered the frequency modulation system and the LABVIEW signal recording/processing subroutines.

In order to study the advantages of the TWR method over conventional PTR, two sets of experiments were designed. First, conventional photothermal radiometry using a software lock-in LABVIEW subroutine [Fig. 13(a)] was performed. In this process, the in-phase waveform is a replica of the incident excitation beam and the quadrature waveform is produced by a Hilbert transform, which shifts the phase of the in-phase component by 90°. Then, using a

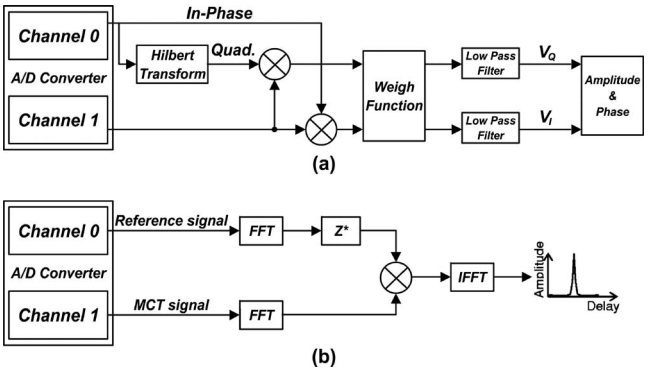

FIG. 13. A flowchart of two signal processing methods used in this study: (a) software lock-in photothermal radiometry and (b) TWR method.

low-pass filter, signals coherent with the reference and the sum frequency in the software mixer (V_I and V_Q for the in-phase and quadrature channels, respectively) are obtained. Finally, the lock-in amplitude and phase can be defined as

$$A = \sqrt{V_I^2 + V_Q^2} \quad \text{and} \quad \varphi = \tan^{-1}(V_Q/V_I). \tag{27}$$

In order to eliminate the instrumental transfer function in our PTR experiments, a reference point located midway between two consecutive holes was chosen as representing a semi-infinite solid and therefore was used to normalize the PTR phase and amplitude channels. The laser beam was expanded to 4 mm to ensure 1D heat diffusion. PTR frequency scans as well as a spatial scan at 5 Hz were carried out over all holes. Next, a high resolution 1×1 mm^2 2D TWR scan was performed on the front surface of the steel sample using the signal processing algorithm shown in Fig. 13(b). The algorithm takes advantage of high-speed FFT routines to compute the cross-correlation function in the Fourier domain, using Eq. (2b), and transforms back to time domain using an inverse FFT algorithm. In order to compensate for the instrumental transfer function, the obtained TWR peak delay times were normalized such that the peak delay time for the semi-infinite sample would be identical to that obtained by the theory. Furthermore, in agreement with the theoretical consideration, we used glass samples painted black on the back surface. Three of the glass samples were Fisher Scientific borosilicate microscope cover slips with thicknesses of 0.12, 0.15, and 0.2 mm. The 1 mm thick glass sample used in our research was a commercial microscope cover slip with unknown physical and optical properties. Using the experimental setup of Fig. 12 and the cross-correlation signal processing technique [Fig. 13(b)], the TWR cross-correlation peak delay time for each glass sample was obtained.

VI. RESULTS AND DISCUSSION

A. Steel sample

Figure 14 shows the results of the frequency-scanned PTR experiments carried out on the steel sample over several holes. In Fig. 14(a), it can be seen that for thicknesses above 600 μm ($l > 600$ μm), the PTR amplitudes are straight lines coinciding with the semi-infinite sample amplitude. The lowest frequency (1 Hz) amplitude of the 1000 μm subsurface hole deviates from the straight semi-infinite line, but is

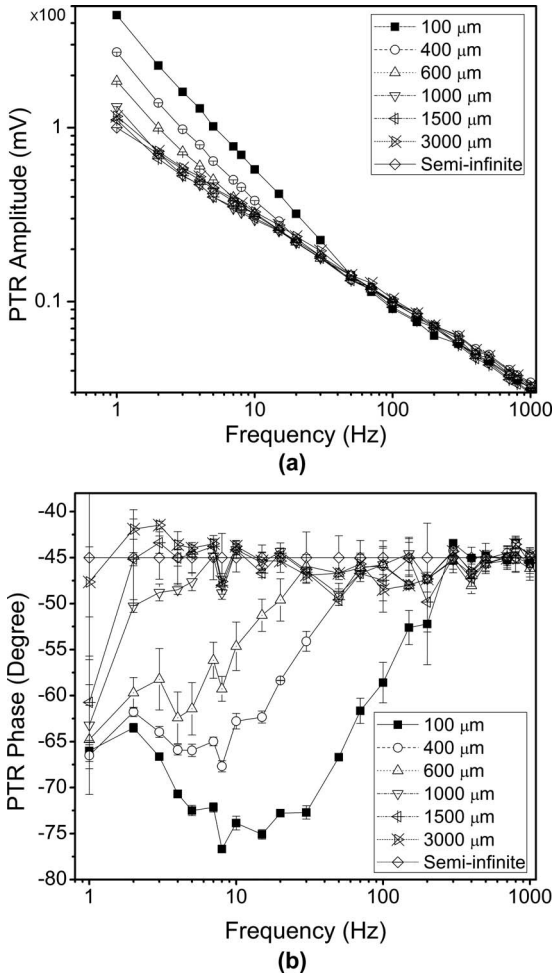

FIG. 14. (a) Log-log amplitude and (b) semi-log phase variation of experimental PTR signal with modulation frequency over subsurface steel sample holes with various depths (as indicated in the inset).

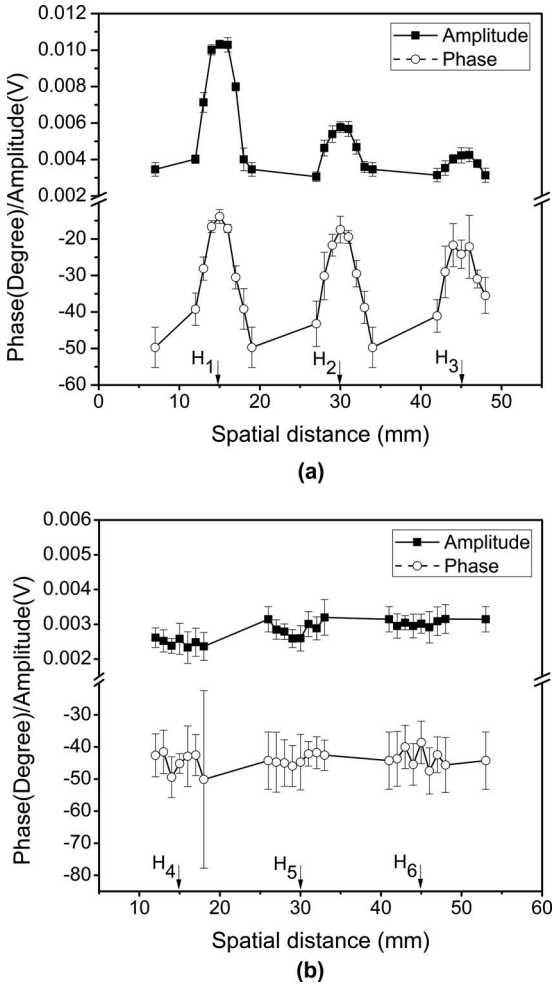

FIG. 15. Experimental amplitude and phase of a spatial scan carried out at 5 Hz over thicknesses of (a) 100, 400, and 600 μm, and (b) 1000, 1500, and 3000 μm (H_j symbols are as schematically shown in Fig. 1 table inset).

within standard deviation of that line. The overlap is more clearly seen in the phase plots [Fig. 14(b)]. It is concluded that the PTR amplitude channel cannot detect inhomogeneities located deeper than 600 μm. Deviation from the semi-infinite sample at lower frequencies over sample thicknesses $l \leq 600$ μm confirms the presence of an inhomogeneity in these samples. As the subsurface hole distance to the surface ($l \rightarrow 0$) decreases, the frequency at which the PTR graph deviates from that of a semi-infinite steel shifts toward higher values. A similar trend can also be seen in the PTR phase response curves. For $l > 1000$ μm, at all scanned frequencies, the PTR phase hovers around the $-45°$ value, which is the theoretical value for a semi-infinite sample, indicating that the PTR phase channel cannot differentiate between these holes and a semi-infinite sample. On the other hand, for $l < 1000$ μm, the PTR phase channel is more highly resolved than the PTR amplitude channel as it can detect samples with identical thicknesses at higher modulation frequencies (shorter thermal diffusion lengths). For example, for $l = 100$ μm, the amplitude channel can only recognize the hole at $f \leq 30$ Hz, but the phase channel can resolve the hole at $f \leq 150$ Hz. This higher accuracy of PTR phase was first reported by Busse and Eyerer.[4] The large error bars in the phase channel at 1 Hz are due to signal cutoff by the ac-coupled preamplifier in our experimental setup. Therefore, despite the ability of the phase channel to resolve the $l = 1000$ μm sample, the experimental results at this frequency may be distorted. In summary, the experimental results suggest that neither of the PTR channels can reliably detect subsurface defects (holes) located deeper than 600 μm.

Figures 15(a) and 15(b) show the results of a conventional PTR spatial scan carried out at 5 Hz along the centerline of shallow ($l = 100$, 400, and 600 μm) and deep ($l = 1000$, 1500, and 3000 μm) rows of holes, respectively. Due to the ac-coupled preamplifier cutoff, the spatial scan at 5 Hz was found to yield optimal results in terms of inhomogeneity detection. The spatial scan can clearly detect the shallow but not the deep subsurface holes. These line-imaging results are consistent with Fig. 14 and show the inability of conventional PTR to detect inhomogeneities deeper than 600 μm.

Figure 16 shows a TWR spatial scan along the same line as Fig. 15. The enhanced dynamic range of TWR can be clearly seen when comparing Figs. 15(b) and 16(b). After normalization of the PTR data with theory (matching the theoretical and experimental delay times of the semi-infinite sample), the TWR delay time can be fitted to the theoretical

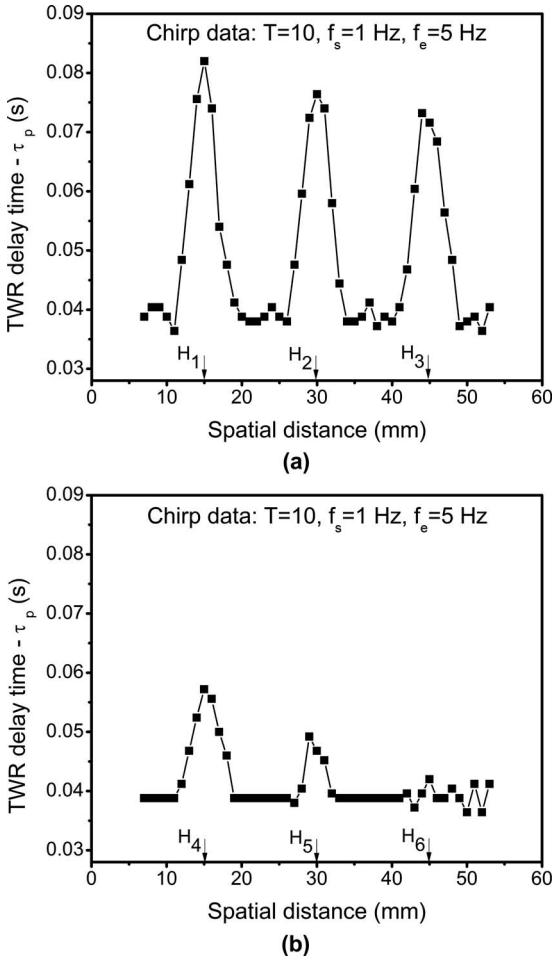

FIG. 16. Experimental TWR spatial scan over thicknesses of (a) 100, 400, and 600 μm, and (b) 1000, 1500, and 3000 μm (H_j symbols are schematically shown in Fig. 1 table inset).

curve to measure the subsurface depth of the holes (Fig. 6, solid line, and open circles, respectively). Figure 17 is a high resolution (1×1 mm^2) TWR image of the steel sample that was obtained through a 2D TWR surface scan. Each pixel represents one laser beam location. The contrast parameter in this image is the cross-correlation peak delay time τ_p. The image is consistent with Fig. 16 in that the TWR can detect holes at distances at least 1500 μm below the surface. This considerable improvement in the depth-resolution dynamic range over conventional PTR is due to the higher SNR of TWR compared to PTR, in agreement with the foregoing

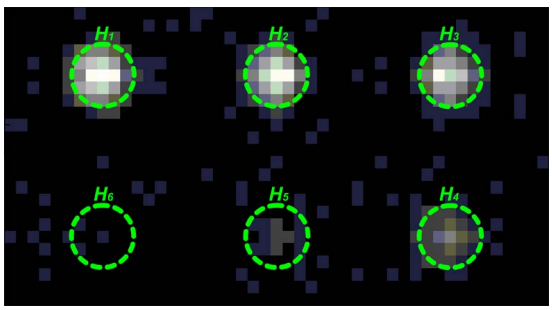

FIG. 17. (Color online) TWR cross-correlation peak delay time τ_p image of the steel sample obtained by running a 2D surface scan. Scanning pixel resolution=1×1 mm^2.

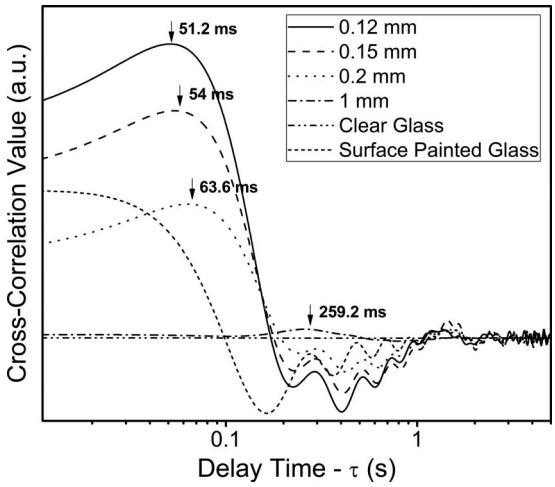

FIG. 18. Experimental TWR cross-correlation peak delay time τ_p as a function of glass sample thickness, as indicated in the figure inset.

theoretical predictions in this paper. As a result, implementation of this method in current PTR imaging modalities can significantly improve the subsurface detection range of such modalities (150% improvement in this case).

B. Back-painted microscope slip glass

Figure 18 shows the experimental TWR results for the glass samples. It should be noted that, for a clear glass sample (not painted on either side), a straight line at zero value indicates that no photothermal signal was obtained from this sample. Therefore, it was concluded that the borosilicate glass used in this research was effectively transparent to the wavelength of the excitation beam. On the other hand, for the front-surface painted glass sample, the absence of TWR cross-correlation maximum indicates purely surface absorption (no delayed conductive contribution from underlayers). For the back-surface painted glass samples, as the thickness of the glass increases, the corresponding conduction peak delay time also increases (as predicted by theory, Fig. 9). Furthermore, with an increase in glass thickness, the TWR signal is strongly reduced as thermal waves decay exponentially across the glass thickness. This effect significantly reduces the SNR and limits the maximum detection range of this method. However, averaging, windowing, and optimizing the excitation chirp parameters are potential solutions to this problem.

The TWR peak delay time τ_p is characteristic of the depth of the absorber and can be empirically fitted to the diffusive equation,

$$\tau_p(l) = k_1 l^2 + k_2, \tag{28}$$

where k_1 and k_2 are unknown constants that can be obtained by fitting the diffusive equation to the simulation data. Equation (28) indicates that imaging performed at fixed delay times τ_p using the TWR will yield a thermal-wave image from a fixed depth l. This feature of the TWR is not matched by conventional frequency-domain thermal-wave imaging (and PTR in particular): fixed τ_p spatial scans using the TWR can lead to depth-selective subsurface images, whereas PTR scans at fixed frequency only lead to depth-integrated sub-

surface imaging down to a distance controlled by the thermal diffusion length. The solid line in Fig. 9 represents the fitted diffusive equation [Eq. (28)] to the simulation data [Fig. 9 (○)]. It can be observed that the normalized experimental data [Fig. 9 (∇)] closely follow the simulated trend. As a result, the simulation fitted diffusive equation can be used to decipher TWR images and obtain depth information of subsurface absorbers.

In summary, a new thermal-wave depth-profilometric and depth selective method based on a linear frequency modulated excitation and matched filter signal processing method (TWR) was introduced. The method is based on radar principles and exhibits enhanced dynamic imaging range (up to 150%) over conventional frequency-scanned thermal-wave PTR imaging. Analytical solutions of the TWR signal were presented. It was found that the ESD of the radiometric signal in finitely thick opaque solids consists of a low-pass filter like spectral energy distribution with distinct superposition contributions from forward thermal waves generated at the sample surface as a result of surface energy absorption and a phase shifted spectral energy distribution that is a function of sample thickness. Simulations of TWR responses from subsurface inhomogeneities have shown that as depth increases, the location of the TWR cross-correlation peak shifts toward shorter delay times. However, in the case of opaque solids, if the spectral energy due to surface absorption is removed from the radiometric signal (TWR subtractive mode), the TWR will only detect the contribution of diffusive waves from underlayers and the dynamic range is significantly improved. In this case, as the sample thickness increases, the TWR cross-correlation peak delay time increases to correspond to a more delayed response from deep underlayers. In transparent solids the radiometric signal ESD is only due to contribution of delayed thermal waves from subsurface absorbers. This effectively amounts to the TWR subtractive mode and can be observed in the TWR delay time versus thickness curve. The experimental results presented in this paper were in agreement with the TWR theory. Moreover, it was found that it is possible to increase the TWR imaging resolution by changing the LFM parameters.

ACKNOWLEDGMENTS

The authors would like to sincerely thank Dr. S. Telenkov and B. Lashkari for their helpful comments and consultations. They are also thankful to Professor R. E. Imhof, South Bank University, for donating the elliptic mirror. The support of the Natural Science and Engineering Research Council (NSERC) and the Ontario Premier's Discovery Award in Science and Engineering is gratefully acknowledged.

[1] G. Busse, Infrared Phys. **20**, 419 (1980).
[2] P. E. Nordal and S. O. Kanstad, Appl. Phys. Lett. **38**, 486 (1981).
[3] A. C. Tam and B. Sullivan, Appl. Phys. Lett. **43**, 333 (1983).
[4] G. Busse and P. Eyerer, Appl. Phys. Lett. **43**, 355 (1983).
[5] A. Mandelis, Solid-State Electron. **42**, 1 (1998).
[6] A. Mandelis, L. Nicolaides, C. Feng, and S. H. Abrams, Proc. SPIE **3916**, 130 (2000).
[7] L. Nicolaides, A. Mandelis, and S. H. Abrams, J. Biomed. Opt. **5**, 31 (2000).
[8] C. H. Kwan, A. Matvienko, and A. Mandelis, Proc. SPIE **6856**, 685625 (2008).
[9] S. A. Telenkov, G. Vargas, J. S. Nelson, and T. E. Milner, Phys. Med. Biol. **47**, 657 (2002).
[10] J. H. Van Vleck and D. Middleton, J. Appl. Phys. **17**, 940 (1946).
[11] G. Turin, IRE Trans. Inf. Theory **6**, 311 (1960).
[12] M. I. Skolnik, *Introduction to Radar Systems* (McGraw-Hill, New York, 1962), Chap. 9.
[13] F. E. Nathanson, *Radar Design Principles: Signal Processing and the Environment* (Prentice-Hall, India, 1999).
[14] E. O. Brigham, *The Fast Fourier Transform* (Prentice-Hall, Englewood Cliffs, New Jersey, 1974).
[15] F. A. McDonald, Appl. Phys. Lett. **36**, 123 (1980).
[16] A. Mandelis Ed, *Principles & Perspectives of Photothermal & Photoacoustic Phenomena* (Elsevier, New York, 1991), Chap. 5, p. 208.
[17] A. Mandelis, L. Nicolaides, and Y. Chen, Phys. Rev. Lett. **87**, 020801 (2001).
[18] A. Mandelis, *Diffusion-Wave Fields, Mathematical Methods and Green Functions* (Springer, New York, 2001), Chap. 2.3, p. 90.
[19] D. P. Almond and P. M. Patel, *Photothermal Science and Techniques* (Chapman & Hall, London, 1996), Chap. 4, p. 94.